Received: Added at production | Revised: Added at production | Accepted: Added at production

DOI: xxx/xxxx

APPLIED RESEARCH

An approach to study recruitment/derecruitment dynamics in a patient-specific computational model of an injured human lung

Carolin M. Geitner*[1] | Tobias Becher[2] | Inéz Frerichs[2] | Norbert Weiler[2] | Jason H. T. Bates[3] | Wolfgang A. Wall[1]

[1]Institute for Computational Mechanics, Technical University of Munich, Garching b. Muenchen, Germany
[2]Department of Anesthesiology and Intensive Care Medicine, University Medical Center Schleswig-Holstein, Campus Kiel, Kiel, Germany
[3]Department of Medicine, University of Vermont College of Medicine, Burlington, Vermont, USA

Correspondence
*Carolin M. Geitner, Institute for Computational Mechanics, Technical University of Munich, Boltzmannstrasse 15, 85748 Garching b. Muenchen, Germany.
Email: carolin.geitner@tum.de

Summary

We present a new approach for physics-based computational modeling of diseased human lungs. Our main object is the development of a model that takes the novel step of incorporating the dynamics of airway recruitment/derecruitment into an anatomically accurate, spatially resolved model of respiratory system mechanics, and the relation of these dynamics to airway dimensions and the biophysical properties of the lining fluid. The importance of our approach is that it potentially allows for more accurate predictions of where mechanical stress foci arise in the lungs, since it is at these locations that injury is thought to arise and propagate from. We match the model to data from a patient with acute respiratory distress syndrome (ARDS) to demonstrate the potential of the model for revealing the underlying derangements in ARDS in a patient-specific manner. To achieve this, the specific geometry of the lung and its heterogeneous pattern of injury are extracted from medical CT images. The mechanical behavior of the model is tailored to the patient's respiratory mechanics using measured ventilation data. In retrospective simulations of various clinically performed, pressure-driven ventilation profiles, the model adequately reproduces clinical quantities measured in the patient such as tidal volume and change in pleural pressure. The model also exhibits physiologically reasonable lung recruitment dynamics and has the spatial resolution to allow the study of local mechanical quantities such as alveolar strains. This modeling approach advances our ability to perform patient-specific studies in silico, opening the way to personalized therapies that will optimize patient outcomes.

KEYWORDS:
lung modeling, reduced-dimensional, recruitment, alveolar strain, VILI, ARDS

1 | INTRODUCTION

Mechanical ventilation is a life-saving therapeutic measure for patients suffering from acute respiratory distress syndrome (ARDS), an often fatal condition that has recently gained widespread attention due to its association with severe cases of COVID-19[1,2]. The main goal of mechanical ventilation is to maintain blood oxygenation and to ensure the removal of carbon dioxide from the lungs. At the same time, mechanical ventilation must be delivered in a manner that minimizes ventilator-induced lung

injury (VILI) and its consequent exacerbation of organ damage [3,4,5]. Two prevailing mechanisms fostering VILI are (i) overdistension of the alveolar tissue, often referred to as *volutrauma*, and (ii) cyclic opening and closure of unstable lung units, often referred to as *atelectrauma* [5,6].

Providing a patient with sufficient minute ventilation while simultaneously minimizing VILI is a challenging task for physicians. For the general ARDS case, various protective ventilation strategies have been developed to reduce the aforementioned injury risks [4] and to improve gas exchange in the lung. Such strategies include the reduction of tidal volume, the application of positive end-expiratory pressure (PEEP), and the use of recruitment maneuvers to open collapsed lung regions. Despite the established clinical benefits of these techniques [7], however, they do not take inter-patient variability into account. This is due in part to the fact that only global parameters of ventilation, gas exchange and respiratory mechanics are typically at hand. Such parameters do not provide insight into the distributed nature of lung injury in what is usually a very heterogeneous pathology. Being able to take both global and local measures of lung function into account when making treatment decisions would be of great benefit to the management of ARDS [8]. The clinical application of electrical impedance tomography (EIT) serves this purpose at the bedside to some extent by deducing regional ventilation distributions based on a map of the electrical properties of the thorax [9]. However, EIT is limited to a slice of the organ (2D-EIT) and has only very coarse resolution. Thus, at the present state of the art, (1) a detailed and comprehensive insight (2) during therapy (3) into the whole lung is not available.

Computational models of the lung that represent ARDS pathophysiology in a personalized manner may thus be helpful in optimizing protective ventilation strategies in clinical practice, especially if they include descriptions of phenomena such as heterogeneous tissue straining and cyclic recruitment of lung units that close during each expiration [8]. Some computational studies have attempted to model the overall recruitment behavior of lungs and show a limited degree of predictive capability [10,11,12]. Due to their single-compartment design, however, they cannot inform about potential sites of regional overdistension caused by tissue inhomogeneity. Multi-compartment models, on the other hand, allow us to investigate the complex dynamics of lung recruitment and derecruitment at a finer level of spatial and temporal scale [13,14,15,16]. In particular, the empirical model of time-dependent recruitment and derecruitment (R/D) dynamics introduced by Bates et al. [15,17,18] has been widely used to interpret experimental data from animal models [16,17,19,20,21,22] and to link R/D dynamics to VILI in certain ventilation strategies [16,18,19,20,21,22,23]. This model has not, however, been incorporated into an anatomically and physiologically realistic representation of the human lung, nor has it been personalized to represent the pathology of an individual patient. In contrast, we have developed a physics-based computational model of the lung [24,25,26] that is able to reproduce the pulmonary ventilation of an ARDS patient over both global and local length scales, but this model does not incorporate a representation of the dynamics of R/D that is so crucial to the fate of a lung with ARDS.

The goal of the present work is therefore to integrate the dynamics of R/D into a comprehensive and anatomically based computational lung model. To do this, we combine our physics-based reduced-dimensional model of the lung based on a realistic morphology [24,25,26] with the afore-mentioned empirical model of R/D dynamics [15,17,18,19,22]. To enhance the physical foundation of the model, the R/D dynamics are related to the dimensions of the airways and to the biophysical properties of the airway lining fluid. This novel modeling approach allows a more realistic estimation of how high-stress sites within the lungs of a given patient might act as foci for the development and propagation of VILI. We evaluate our new model by matching its mechanical behavior to clinical data from a patient suffering from ARDS, and then we used the model to simulate several ventilation maneuvers undertaken at the bedside. Our goal is to develop a tool for creating personalized therapies for the mechanically ventilated patient.

2 | MATERIALS AND METHODS

To set up our patient-specific computational model, information about lung geometry and pulmonary pathophysiology is extracted from clinical data and we further used the data to calibrate the mechanical behavior of the model to that of the patient (see schematic outline in Figure 1).

2.1 | Clinical data

We used chest CT images and ventilation data acquired during the medical treatment of a critically ill, endotracheally intubated 50 year-old female patient suffering from ARDS who was included in another study [27]. The data were provided in an anonymized format by the Department of Anesthesiology and Intensive Care Medicine at Christian Albrechts University in Kiel. Ethical

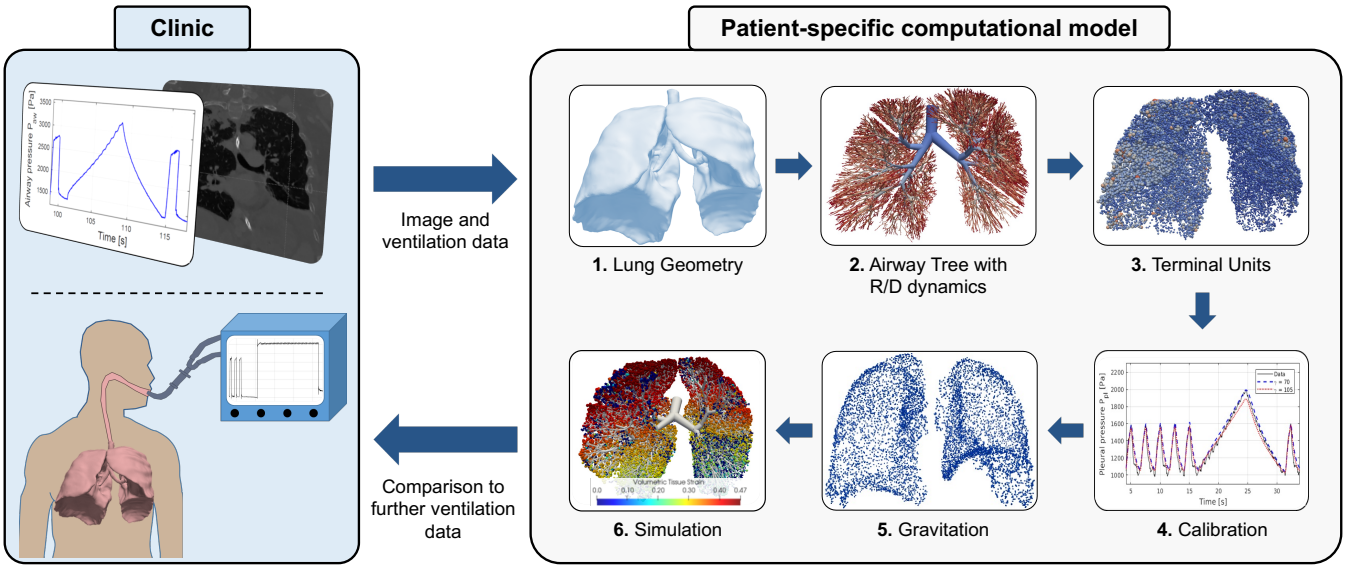

FIGURE 1 Schematic overview of the process to generate the patient-specific computational model of the lung from clinical data to simulate various ventilation profiles and to retrospectively compare it to the clinical reference measures.

approval was obtained from the ethics committee of the Medical Faculty in Kiel, and the underlying study was carried out in accordance with the Declaration of Helsinki.

Image data A single three-dimensional thoracic CT scan of the patient provides the overall geometry for the lung model and allows us to identify derecruited, and thereby potentially recruitable, regions. The scan (512x512x1062 pixels each having dimensions 0.98x0.98x0.7mm) was recorded at a PEEP of 10 mbar (PEEP10). Exemplary views of the lung showing the heterogeneous injury of the organ are depicted in Figure 2.

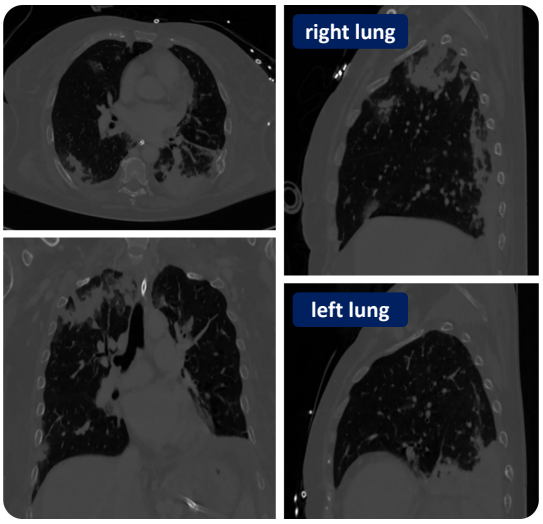

FIGURE 2 CT scan of the patient in axial, coronal and sagittal (right and left lung) view exhibiting heterogeneous lung regions.

Ventilation data Various ventilation profiles were applied to the patient at the bedside to reveal the specific mechanical properties of the respiratory system and to adapt the ventilation parameters appropriately for therapy. Measurements included

the pressure at the airway opening, the tracheal air flow entering the lung, and esophageal pressure as a surrogate for pleural pressure. Transpulmonary pressure (P_{tp}) was calculated as the difference between tracheal and esophageal pressures.

2.2 | Reduced-dimensional lung model

Our computational study is based on the previously developed reduced dimensional computational model[24,25,26] extended to include a well-investigated model of R/D dynamics[15,17,18]. In the following, we briefly restate the central components of these models.

2.2.1 | Model geometry

Using the CT image, we identified the centerline of the visible parts of the airway tree from distal end of the endotracheal tube down to the lobar bronchi. The individual lobes of the lung were segmented (Mimics and 3-Matic, Materialise, Leuve, Belgium) and the airway branches within each lobe generated by a space-filling algorithm[26,28]. The recursive branching of a parent airway into two daughter airways follows morphological length and diameter ratios[29,30,31] and terminates when either

- the length of an airway is smaller than 1.2 mm,
- the diameter of an airway is smaller than 0.4 mm,
- a maximal number of 17 generations is reached, or
- the hull geometry of the segmented lobe is penetrated.

The resulting three-dimensional airway tree mimics the purely conducting zone of the lung and is modeled by reduced-dimensional airway elements (see Section 2.2.2). At each terminal branch, we attach a so-called *terminal unit* (see Section 2.2.3). These terminal units represent the remaining smaller tissue structures reaching into the parenchymal region beyond the conducting airway tree. In total, the model contains 48,178 reduced airway elements and 24,089 terminal units.

2.2.2 | Conducting airways

0D airway model Each branch of the tracheo-bronchial tree is modeled by a reduced-dimensional element reproducing the averaged behavior of flow and wall mechanics in a fully resolved, elastic, three-dimensional airway, closely following Ismail et al.[26]. The rates of inflow Q_{in} and outflow Q_{out} of a 0D airway are driven by the pressure drop $\Delta P = P_{in} - P_{out}$ across the element and the external pressure, $\widetilde{P}_{ext}$, and are determined by

$$\begin{aligned} C\frac{\mathrm{d}}{\mathrm{d}t}\left(\frac{1}{2}\left(P_{in}+P_{out}\right)-\widetilde{P}_{ext}\right)+Q_{out}-Q_{in}+C\cdot R_{visc}\frac{\mathrm{d}}{\mathrm{d}t}\left(Q_{out}-Q_{in}\right)=0,\\ \frac{I}{2}\frac{\mathrm{d}}{\mathrm{d}t}\left(Q_{in}+Q_{out}\right)+\frac{1}{2}\left(R_{\mu}+R_{conv}\right)\cdot Q_{out}+P_{out}-P_{in}=0, \end{aligned} \tag{1}$$

where C is the capacitance of the airway wall, R_{visc}, R_{conv} and R_{μ} are the visco-elastic, convective and nonlinear airway resistances, respectively, and I is inductance. For further details on these quantities see[24,25,26].

R/D dynamics of airways To include time-dependent R/D dynamics in our patient-specific model of the lung, we followed the semi-empirical and established approach introduced by[15,17,18]. The approach assumes that an individual (de-)recruitable airway can either be completely open (state = 1) or completely closed (state = 0), and switches between these states depending on the pressure it is exposed to and the duration of this exposure. The transitions between the two states are modeled using a variable x that moves along a virtual trajectory between 0 and 1 according to

$$\frac{\mathrm{d}x}{\mathrm{d}t}=\begin{cases} s_o(P_{in}-P_o) & P_{in}>P_o \\ s_c(P_{in}-P_c) & P_{in}<P_c \\ 0 & else, \end{cases} \tag{2}$$

where P_o is the critical opening pressure, P_c is the critical closing pressure, and s_o and s_c are constants of proportionality. When P_{in} exceeds P_o, x moves toward 1. If P_{in} falls below P_c, x approaches 0. The rate at which x changes depends both on the constants s_o and s_c and on the difference between P_{in} and the corresponding critical pressure. If x reaches 0 when the airway is open, or 1 when the airway is closed, closure or opening is triggered, respectively. When $0 < x < 1$, the state of an airway

does not change. When $P_c < P_{in} < P_o$, x remains constant. Following [15], we model a closed 0D airway element by setting its resistance to a high value of $R_\mu = 10^{16}$kg/s.m^4 in Equ. (1), which effectively eliminates airflow through it. Further details on the model can be found in [15,17,18].

In previous works employing this dynamic R/D model, the values of the model parameters in Equ. (2) have generally be determined in a stochastic manner [15,17,18], which represents the complex mechanical events occurring in an airway during reopening in purely phenomenological terms. In contrast, we try to base the parameters of our composite model on physical relationships as far as possible. Thus, based on experimental findings [32], we compute P_o for an airway using its radius r_{aw} and the surface tension, γ, of its lining fluid according to

$$P_o = 8.3\frac{\gamma}{r_{aw}}. \tag{3}$$

Since the composition of the lining fluid in a diseased lung region is unknown, we consider three different values for γ in Equ. (3). As one reasonable choice, we assume the fluid to be dominated by human serum albumin, a major component of human blood plasma, with a surface tension of $\gamma = 70$ dyn/cm [33]. This protein is presumably also present in airways damaged by inflammatory processes and cyclic reopening [34], resulting in epithelial cell damage and leakage of blood plasma into the air spaces. As the airway fluid might also transition to stickier sputum [35], we consider two additional arbitrarily chosen scenarios of $\gamma = 100$ dyn/cm and $\gamma = 130$ dyn/cm.

We choose P_c in Equ. (2) 4 cmH_2O lower than the corresponding P_o according to [18]. The constants s_o and s_c that influence the rate of airway opening and closing, respectively, are assumed to follow the quasi-hyperbolical distributions $s_o \in \frac{S_o}{\text{unif}[0,1]}$ and $s_c \in \frac{S_c}{\text{unif}[0,1]}$ [18]. Herein, unif$[0, 1]$ describes uniformly distributed stochastic values between 0 and 1. S_o and S_c are constants set to 0.04 cm$H_2O^{-1}s^{-1}$ and 0.004 cm$H_2O^{-1}s^{-1}$, respectively [18]. Finally, s_o and s_c are coupled such that $s_o = 10s_c$ for each collapsible airway.

To account for the patient-specific spatial heterogeneity of the diseased lung in our computational model, we apply the above time-dependent R/D model to those airways of the tracheo-bronchial tree that are located in injured (i.e., non- or poorly-aerated) regions of the lung. The potentially atelectatic regions are identified in the CT scan as having Hounsfield Units (HU) > -300 [36]. All airways distal to a collapsible airway are assumed to be of a similarly diseased state (e.g., due to abnormal liquid lining properties and/or restricted airflow) and are therefore also subjected to R/D in our model. Figure 3 shows all 18,952 airways of the airway tree that are collapsible based on the conditions described above. The distributions of P_o for all collapsible airways,

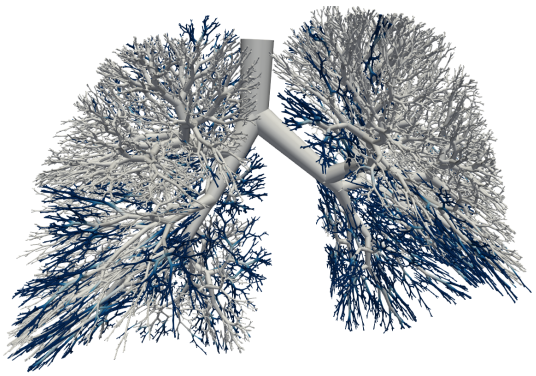

FIGURE 3 Generated airway tree with (de-)recruitable airways (blue) identified by regions in CT scan with densities above -300 HU.

following Equ. (3), are depicted in Figure 4 for each γ.

2.2.3 | 0D terminal units

The terminal units comprising the respiratory zone beyond the distal ends of the conducting airway tree are represented by generalized Maxwell models that reproduce the nonlinear viscoelastic behavior of alveolar tissue [26]. A hyperelastic compressible Ogden-type material law [37] is used to model the nonlinear elastic behavior of the lung parenchyma [24], derived by assuming pure

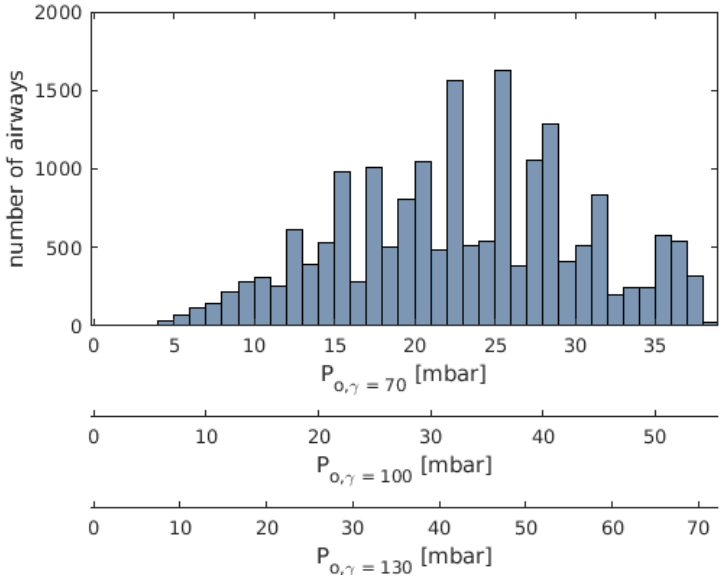

FIGURE 4 Distribution of the critical opening pressures $P_{o,\gamma}$ of all recruitable airways with respect to the three investigated values for the surface tension γ, 70 dyn/cm, 100 dyn/cm and 130 dyn/cm.

volumetric deformation as

$$P_{alv} - P_{pl} = \frac{\kappa}{\beta} \cdot \frac{V_{0,unit}}{V_{unit}} \left(1 - \left(\frac{V_{0,unit}}{V_{unit}} \right)^{\beta} \right), \tag{4}$$

where V_{unit} is the current volume of a terminal unit, $V_{0,unit}$ is the reference value of V_{unit} in the stress-free state, P_{alv} is alveolar pressure, and P_{pl} is pleural pressure. The slope and shape determining parameters κ and β, respectively, define the material properties of the lung tissue. κ and β are estimated for the lungs of a specific patient by a fitting procedure (Section 2.2.5).

When determining $V_{0,unit}$ for each terminal unit, we have to consider the heterogeneous nature of a damaged lung. The terminal units are mechanically independent and thus generally exist in different mechanical states, either collapsed and presumably stress-free or normally inflated and thus distended. We cannot therefore simply calculate the total lung volume from the CT image by solving Equ. (4) and distributing it evenly across all terminal units because this could underestimate local increase in volume capacity resulting from recruitment. We therefore split the total volume of each lobe, derived from the CT image, into two parts, one consisting of air and the other of tissue based on HU = -1000 for air and HU = 0 for water ($\sim$ tissue)[38].

The volume of the part comprised of water is assumed to correspond to the volume of the lobar tissue, $V^{tissue,lb}$. We distribute $V^{tissue,lb}$ across all lobar terminal units in proportion to the area, A^{lb}_{unit}, of the airway supplying each unit, which was set during the tree growing procedure. A^{lb} is the sum of all the individual A^{lb}_{unit} for the lobe. That is, $V^{tissue}_{unit} = V^{tissue,lb} \cdot A^{lb}_{unit} / A^{lb}$. This approach is motivated by the assumption that larger airways support larger alveolar regions. To get the total volume of a terminal unit, including both its air and tissue volumes, we distribute the total air volume of the lung across all terminal units so as to recreate their respective HU in the CT image. The total volume of a terminal unit determined in this way corresponds to the volume $V_{unit,CT}$ of the unit under the pressure load at the time of the CT scan, i.e., with PEEP10 applied at the airway opening and the corresponding pleural pressure. The reference volume $V_{0,unit}$ of open terminal units can then be calculated by solving Equ. (4). Initially trapped terminal units, i.e., units that are attached to an initially collapsed airway, are assumed to be nearly collapsed, and therefore already in a stress-free state so that $V_{0,unit} = V_{unit,CT}$.

2.2.4 | Pressure boundary conditions

The external pressure acting on a terminal unit has two components: 1) a volume-dependent component P^{vol}_{pl} due to the elastic recoil of the chest wall, and 2) a static component P^{weight}_{pl} due to the weight of the lung that is above the units in question. The pleural pressure is the sum of these two components, that is: $P_{pl} = P^{vol}_{pl} + P^{weight}_{pl}$. P^{vol}_{pl} is determined by the total volume of all

terminal units and thus implicitly integrates the passive mechanical properties of the sedated chest wall into the model. Since the relationship between the lung volume and P_{pl} during a quasi-static inflation maneuver is linear over most of its typical range (Figure 5b, see more details in Section 2.2.5), we match the linear relationship

$$P_{pl}^{vol} = P_{pl,0} + P_{pl,lin} V_{frac}, \tag{5}$$

with

$$V_{frac} = \frac{(V - V_{PEEP})}{(V_{max} - V_{PEEP})} \tag{6}$$

to clinical measurements by determining $P_{pl,0}$ and $P_{pl,lin}$ accordingly. The volume fraction V_{frac} describes the ratio between the increase in volume, $V - V_{PEEP}$, from the volume level at PEEP10, calculated from the CT scan, and the increase in volume during the quasi-static inflation maneuver at end-inspiration, $V_{max} - V_{PEEP}$.

P_{pl}^{weight} is the pressure across a section of lung tissue due to the weight of the lung above it, treating the organ as a fluid body subjected to gravity. This weight is usually larger in an ARDS compared to a healthy lung because of the extra fluid accumulation. To include this effect in our model, we employ the relation proposed in[39] that provides the pressure resulting from the weight of the lung as a function of ventral-to-dorsal height of the lung, h_{lung}:

$$P_{pl}^{weight} = 0.541 \cdot (h_{lung} - h_{balloon}) + 0.015 \cdot (h_{lung}^2 - h_{balloon}^2). \tag{7}$$

To achieve a static pressure of zero at the reference point of measurement, which is made using an esophageal balloon, we determine the height of the measurement site, $h_{balloon}$, from the CT image[40] and introduce it into Equ. (7).

2.2.5 | Patient-specific parameter calibration

At an overall level, the respiratory system is composed of two distinct interacting sub-systems, the lung and the chest wall[41]. In order to personalize these two sub-systems to the patient in this study, we fit the remaining parameters of Equ. (4) (i.e., κ and β) and Equ. (5) (i.e., $P_{pl,0}$ and $P_{pl,lin}$) to recordings of pressures and volume made during a quasi-static inflation maneuver starting at PEEP10. The low flow employed during this maneuver minimizes viscous effects in the lung tissue, so the resulting pressure-volume curve is largely reflective only of the elastic behavior of the respiratory system. Both equations were fit to the inspiratory segments of the pressure-volume data in MATLAB using a nonlinear regression method (see Figure 5).

In our model, the lung sub-system can be viewed as the collective behavior of all terminal units (see Section 2.2.3). As their deformation is governed by the interplay of the alveolar and pleural pressures, we fit κ and β to the transpulmonary pressure $P_{tp} = P_{alv} - P_{pl}$ and the corresponding lung volume in the quasi-static inflation maneuver (Figure 5a). We assume κ and β to be the same for all terminal units. The heterogeneity of the diseased lung is accounted for by collapsible airways. That is, when an airway is closed its downstream tissue units no longer communicate with the airway opening (i.e., these units become derecruited). As a consequence, the model stiffens regionally.

Accordingly, we estimate the parameters of P_{pl}^{vol} (Equ. (5)) such that we can reproduce the P_{pl}-V behavior of the quasi-static inflation maneuver (Figure 5b). The values of the parameters describing the elastic material behavior of the terminal units and the pleural pressure conditions are given in Table 1.

3 | RESULTS

Simulation protocol To investigate the behavior of our model in a real-life scenario, we simulated a 28-minute long recording of the patient's ventilation protocol at the bedside. The model was driven by the airway pressure applied during mechanical ventilation. Note that the simulated ventilation patterns do not include the quasi-static inflation maneuver from PEEP10 that was used to calibrate the model (Section 2.2.5), so the maneuvers used to validate the model are not the same as that used to develop it.

We used the following maneuvers for validation:

1. cycles of normal ventilation containing two quasi-static inflation maneuvers with different peak pressures, starting from PEEP16 (Figure 6),

2. cycles of normal ventilation at PEEP13 with half the original driving pressure (Figure 7), and

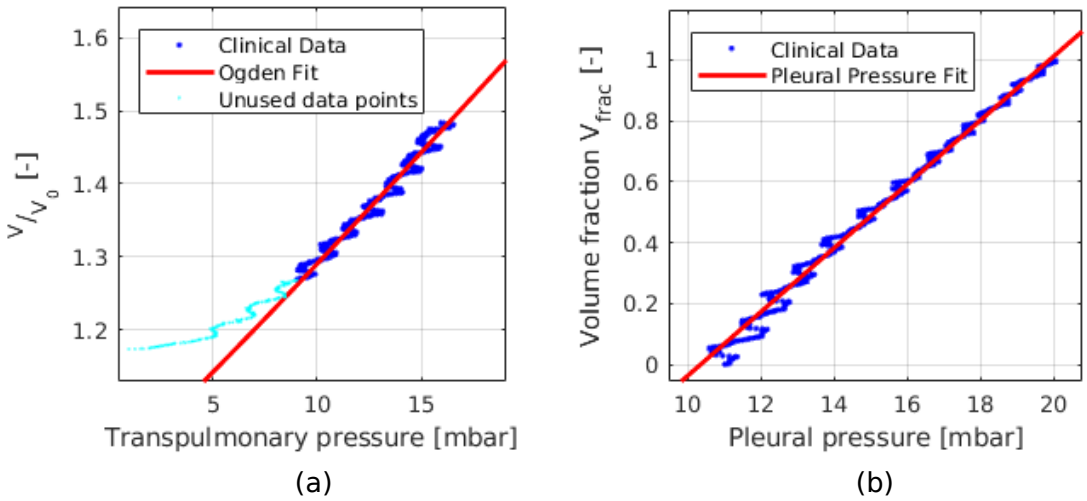

FIGURE 5 (a) Pressure-volume curve of all terminal units (red) calibrated to the clinical measurement of transpulmonary pressure and volume (blue), and (b) relation between the volume fraction and the pleural pressure used as boundary condition in the model (red) determined from the measured pleural pressure-volume-curve (blue). Data points in (a) below the lower inflection point (light blue) have been neglected for the calibration as the curvature of this part might result from recruitment effects and, thus, not exhibit the pure elastic pressure-volume behavior of the lung.

3. a sustained-inflation maneuver starting at PEEP16 in which the airway pressure was maintained at 40 mbar for a period of ∼32 seconds, followed by ventilation at elevated PEEP19.

The chronological order of these maneuvers is indicated by the time indications in the figures. We simulated these maneuvers for three different values of γ of 70, 100, and 130 dyn/cm. As we did not know the initial state of each collapsible airway, we chose $P_o > 24$ mbar as the critical threshold for airways to be declared closed initially. This value minimizes the transient opening and closing of airways during the first simulated ventilation cycles with PEEP10 and an end-inspiratory pressure of 32 mbar. We simulated several additional normal ventilation cycles at the beginning of each run to achieve steady state.

Global ventilation quantities Figures 6 - 8 show the responses of relevant ventilation characteristics to the applied airway pressure profiles (top) over time. These include (from top to bottom): (i) air flow-derived tidal volume, (ii) comparison of measured and simulated P_{pl}, and (iii) the percentage of open airways. Our simulated results show good agreement with the clinical measurements for all chosen values of γ. Nevertheless, as expected, the system is sensitive to the choice of γ. In particular, a higher value of γ leads to elevated and more broadly distributed values for P_o (Figure 4), which results in reduced tidal volumes and reduced swings in P_{pl} due to fewer reopened tissue regions (terminal units). We observe this effect in all investigated ventilation profiles at end-inspiration (Figures 6 - 8).

For the normal ventilation cycles (Figure 6) and the quasi-static inflation maneuver, the clinical data are best reproduced by the model for $\gamma = 100$ dyn/cm, particularly as regards tidal volume. Assigning γ the value for human albumin of 70 dyn/cm leads to slight overestimations of tidal volume and swings in pleural pressure. When the driving pressure is reduced by 50%, the tidal volume approximates clinical measurements at the peak of inspiration well (Figure 7). Nevertheless, there remains some mismatch between measured and simulated tidal volumes for all values of γ investigated. The simulated and measured sustained-inflation maneuvers show good agreement both in terms of tidal volume and change in pleural pressure for $\gamma = 100$ dyn/cm, including their time-dependent, continuous increase (Figure 8). However, the simulated drop in pleural pressure and especially the observed simultaneous decrease in lung volume after this maneuver diverge from the clinical data. Elevations in both quantities are expected because of the raising of PEEP from 16 to 19 mbar, which would increase the volume capacity of the lungs due to both stronger distension and recruitment. The discrepancies between the simulations and the data

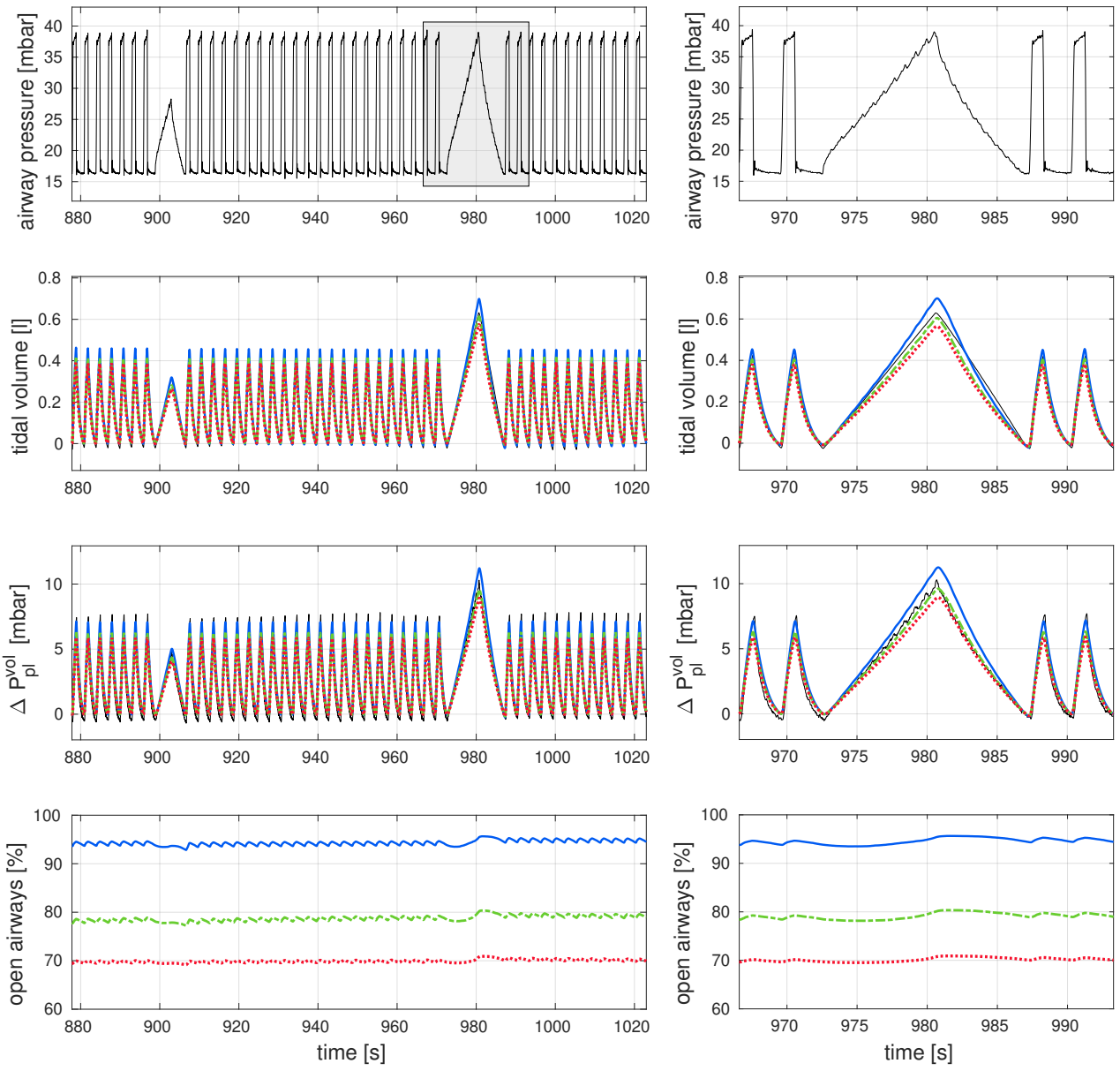

FIGURE 6 Simulation results of the proposed computational model for a clinically applied airway pressure profile of normal ventilation alternated by two quasi-static low-flow inflation maneuvers (top) for all three scenarios of surface tension γ, 70 dyn/cm (blue solid), 100 dyn/cm (green dashed) and 130 dyn/cm (red dotted) from top to bottom: tidal volume and change in pleural pressure compared to the clinical measurements (black solid), and the percentage of open airways in the whole model; in each figure, the area highlighted in grey (top left) indicates the period shown in more detail in the right column for all mentioned measures.

could thus indicate that airways close too slowly in our model. This would allow air to escape from the lungs prior to closure and thus to reduce gas trapping. In addition, the differences between simulation and data differ for tidal volume and pleural

pressure after the recruitment maneuver. This might suggest erroneous measurement of the very high flows occurring just after release of the high pressure, something that we also observed subsequent to other simulated recruitment maneuvers (data not shown), where the simulated pleural pressure behaves similarly to the recordings at the bedside, yet, the tidal volume does not.

R/D and underlying time dependence In general, the R/D processes in our model occur continuously during ventilation and behave as expected. For example, the number of open airways changes depending on the applied airway pressure. A drop in pressure results in the gradual closure of airway elements, and vice versa. On the time scale of a single breath, we observe intra-tidal R/D in our model indicated by a varying number of open airways throughout each breath (see, e.g., normal ventilation in Figure 6). On the timescale of the overall ventilation protocol, we see that a reduction in driving pressure and, thus, of the tidal volume leads to less intra-tidal reopening indicated by a decreased amplitude of oscillations in the number of open airways compared to normal ventilation cycles (Figure 7).

R/D dynamics are strongly influenced by γ (Figures 6 - 8), with a lower value of γ resulting in more airways being permanently open. Moreover, changing γ causes a change in the number of airways that transition between open/closed states with a change in ventilation modality. For example, during the second quasi-static inflation maneuver shown in Figure 6, about ∼1.4 % of the airways recruit in the model with the highest γ compared to ∼2.2 % of the airways in the model with the lowest γ. We also observe this sensitivity of R/D to γ in the rates at which airways close when the driving pressure is suddenly halved (Figures 7), and during the period of constant PEEP immediately prior to a sustained inflation maneuver (Figure 8). The effect is most pronounced with the lowest γ even though the most airways remain open because of the concomitant change in P_o; increasing γ widens the distributions of P_o and P_c and moves both to higher pressures (Figure 4). The effects of γ on R/D magnitude and dynamics are thus somewhat complex.

The importance of including time dependence of R/D in the model becomes apparent when simulating the sustained-inflation maneuver. Here, the simulated gradual increases in lung volume and the number of open airways match observations well for $\gamma = 100$ dyn/cm (Figure 8) and show that recruitment is still continuing at the end of the maneuver. In contrast, for $\gamma = 70$ dyn/cm, all airways reopen almost immediately after the increase in pressure, allowing the lung to reach its full capacity quickly.

Finally, our model shows permanent (de-)recruitment effects after certain maneuvers. Subsequent to the larger quasi-static inflation maneuver (Figure 6), the number of open airways during normal ventilation remains slightly increased even though PEEP and driving pressure have returned to their pre-maneuver settings. This shows that temporary recruitment maneuvers can have a permanent beneficial effect on the amount of open lung. By the same token, the model also reproduces the opposite effect; when driving pressure is temporarily decreased there can be a permanent reduction in the amount of open lung (Figure 7).

Local tissue strain Our reduced-dimensional, yet spatially resolved, modeling approach enables us to study local tissue mechanics in the lung. Of particular interest in this regard is the strain that is experienced by different lung regions depending on local ventilation and gravitational loads. Since the model with $\gamma = 100$ dyn/cm shows the best agreement with clinical data (Figures 6 - 8), we focus on this value of γ in the following. Figures 9 and 10 show the tissue strains in the terminal units at selected points along the simulated airway pressure profile. At each point, an averaged global strain is determined as the ratio between current lung volume in the computational model and the end-expiratory lung volume of 3.21 l calculated from the CT image. This helps to illustrate discrepancies between the observed global strain (marked on the color bars) and the actual local strains.

Figure 9 depicts the local volumetric tissue strains derived from our model during normal ventilation and at the end of the subsequent maneuver with temporarily reduced driving pressure, at two points within the breath. As expected, strains are higher during normal ventilation at peak-inspiration. However, we also see a slightly reduced end-expiratory lung volume (EELV) at end-expiration when driving pressure is halved. This mainly results from the viscous behavior of the terminal units; because tidal volume is reduced but the inspiration/expiration time ratio remains fixed, viscoelastic creep allow the terminal units to contract further than would be the case in normal ventilation mode. Thus, not all dynamic phenomena in the model are attributable to R/D. Nevertheless, Figure 10 also shows explicit effects of recruitment as the number of open terminal units changes throughout the course of the sustained inflation. Importantly, in contrast to the monitored global strain, the model reveals the existence of potentially harmful regional strains above 1.5[42,43].

Another phenomenon captured by our model is gas trapping. This occurs predominantly in regions of inhomogeneity where one can observe terminal units that have a constant strain level over a wide range of ventilation states (Figures 9 and 10). It is only during a recruitment maneuver that these units finally open up.

4 | DISCUSSION

In this study, we propose an approach for comprehensively modeling the ventilatory response of a patient suffering from ARDS. Our previously described physics-based reduced-dimensional computational model based on patient-specific morphological information[24,25] is combined with an established empirical model of airway R/D dynamics[15,17,18,19,22,44]. We extended the R/D model by linking the critical opening pressures of closed airways to the biophysical effects of surface tension in the airway lining fluid[32] and the dimensions of the tracheo-bronchial tree determined from a thoracic CT image[28]. The CT image also allowed us to apply the R/D model specifically to diseased regions of the lung, thereby taking regional heterogeneity of lung function into account. Finally, we account for gravitational effects on the lung tissue.
Compared to other models in the literature[20,21,45,46], the model we have developed here is the first mechanically based and spatially resolved computational description of the entire lung that incorporates R/D dynamics and can be tailored to a specific human lung.

We parameterized the elastic behavior of the tissue elements in the model in a personalized manner by matching its behavior to that measured in a ventilated patient[24], focusing on a quasi-static inflation maneuver in order to calibrate the model to a wide range of pressure and volume behavior. We also accounted for the influence of the thoracic cage with a pressure boundary condition corresponding to the measured esophageal pressure that was a function of lung volume. We tested the computational model by comparing its predictions to pressure, flow and volume data measured in the mechanically ventilated ARDS patient during various respiratory maneuvers. The model recapitulated the key features of the measured data (Figs. 6 - 8). The model also reproduced the dynamic R/D phenomena that led to phenomena such as gas trapping, transient opening and closing of airways, and repetitive intra-tidal recruitment, all of which may play an important role in the generation of ventilator-induced lung injury.

A particularly novel aspect of our model is that it allows the investigation of the effects of surface tension on the dynamics of R/D. The best match of the model predictions to experimental measurement was obtained with $\gamma = 100$ dyn/cm (Figs. 6 - 8) both in terms of lung compliance and the transient increase in lung volume seen during a sustained inflation maneuver. Since the composition of the airway liquid, and consequently the value of γ, are likely to depend on ARDS severity, choosing the value of γ appropriately is clearly critical to model performance. This is perhaps most crucial in terms of the degree of cyclic R/D taking place within the breath, since this is likely a potent mechanism for causing lung injury. In particular, a high proportion of cyclic R/D in the model may indicate the potential for harmful shear stresses to occur at airway walls[34] and thus might be taken as an indicator for the contribution of atelectrauma to VILI[47]. Simultaneously, the model provides insight into potential risk of volutrauma by revealing local strains.

Despite its advantages, however, the model also has some limitations. Since the composition of pathologic airway lining fluid is unknown, we assumed the same fluid properties for all diseased sites in the lung. This neglects any local changes in surface tension that might arise, for example, as a consequence of changes in the types and proportions of airway fluids that are present, or as a result of varying pathological states within the lung[35]. Nor do we consider the changes in production and secretion and the degradation of surfactant in pulmonary diseases[48]. Even the average value of γ may vary among patients and between different pathological conditions and will therefore likely be difficult to determine in any specific case. Thus, the choice of the physically important parameter γ may have to be made on the basis of the clinical history of the patient and current conditions within the lung such as newly emerging versus long-term atelectasis along with any information that can be obtained about the ease with which collapsed lung can be recruited. Uncertainty quantification based on quantitative assessment of the effects of variations in the value of γ in the model will therefore likely be important. Methods of uncertainty quantification continue to advance and are proving valuable in dealing lack of knowledge in biomedical systems[49,50]. Another model limitation is that we only considered R/D at the airway level, yet collapse and reopening also occurs in the alveolar regions[20,51]. Thus, the terminal components of our model cannot mimic intermediate states of tissue distension such as might occur under pathological conditions[20,21] as opposed to being either fully closed or open according to Equ. (4). Tackling these various shortcomings are promising future research objectives. In addition, using the model to make quantitative estimations of the propagation and degree of VILI caused by cyclic opening and closing and/or over-distension will be a crucial step toward optimizing mechanical ventilation in a patient-specific manner[8].

5 | CONCLUSION

In conclusion, we have introduced a novel approach to modeling the lung in a physics-based and spatially resolved manner. The model includes an empirical mechanism for R/D that is linked to airway dimensions and liquid lining properties. We applied this approach to the simulation of lung dynamics in an ARDS patient receiving mechanical ventilation in the intensive care unit. The model recapitulates the key features of the measured airway pressure, flow and volume, and provides insight into local inhomogeneity of lung function that manifests during varying pressure conditions. The model thus has the potential to elucidate spatial distributions of damaging mechanisms throughout the lung that may lead to ventilator-induced lung injury. This represents an important step toward the development of individualized therapies for the ARDS patient.

ACKNOWLEDGEMENTS

We gratefully acknowledge financial support by the Deutsche Forschungsgemeinschaft (DFG, German Research Foundation) in the project WA1521/26-1, by BREATHE, a Horizon 2020—ERC–2020–ADG project (grant agreement No. 101021526-BREATHE), and by NIH grant R01 HL142702.

DISCLOSURES

Wolfgang A. Wall is chief scientific advisor and co-founder of Ebenbuild GmbH.

References

1. Li X, Ma X. Acute respiratory failure in COVID-19: Is it "typical" ARDS?. *Critical Care* 2020; 24(1): 1–5. doi: 10.1186/s13054-020-02911-9

2. Fan E, Beitler JR, Brochard L, et al. COVID-19-associated acute respiratory distress syndrome: is a different approach to management warranted?. *The Lancet Respiratory Medicine* 2020; 8(8): 816–821. doi: 10.1016/S2213-2600(20)30304-0

3. Gattinoni L, Carlesso E, Cadringher P, Valenza F, Vagginelli F, Chiumello D. Physical and biological triggers of ventilator-induced lung injury and its prevention. *European Respiratory Journal, Supplement* 2003; 22(47): 15–25. doi: 10.1183/09031936.03.00021303

4. Slutsky AS, Ranieri VM. Ventilator-Induced Lung Injury. *New England Journal of Medicine* 2013; 369(22): 2126–2136. doi: 10.1056/NEJMra1208707

5. Beitler JR, Malhotra A, Thompson BT. Ventilator-induced Lung Injury. *Clinics in Chest Medicine* 2016; 37(4): 633–646. doi: 10.1016/j.ccm.2016.07.004

6. Bates JHT, Smith BJ. Ventilator-induced lung injury and lung mechanics. *Annals of Translational Medicine* 2018; 6(19): 378–378. doi: 10.21037/atm.2018.06.29

7. The Acute Respiratory Distress Syndrome Network . Ventilation with Lower Tidal Volumes as Compared with Traditional Tidal Volumes for Acute Lung Injury and the Acute Respiratory Distress Syndrome. *New England Journal of Medicine* 2000; 342(18): 1301–1308. doi: 10.1056/NEJM200005043421801

8. Kollisch-Singule MC, Jain SV, Andrews PL, et al. Looking beyond macroventilatory parameters and rethinking ventilator-induced lung injury. *Journal of Applied Physiology* 2018; 124(5): 1214-1218. PMID: 29146685doi: 10.1152/japplphysiol.00412.2017

9. Frerichs I, Amato MBP, Kaam vAH, et al. Chest electrical impedance tomography examination, data analysis, terminology, clinical use and recommendations: consensus statement of the TRanslational EIT developmeNt stuDy group. *Thorax* 2017; 72(1): 83–93. doi: 10.1016/j.imu.2018.06.003

10. Nabian M, Narusawa U. Patient-specific optimization of mechanical ventilation for patients with acute respiratory distress syndrome using quasi-static pulmonary P-V data. *Informatics in Medicine Unlocked* 2018; 12(April): 44–55. doi: 10.1016/j.imu.2018.06.003

11. Morton SE, Knopp JL, Tawhai MH, et al. Prediction of lung mechanics throughout recruitment maneuvers in pressure-controlled ventilation. *Computer Methods and Programs in Biomedicine* 2020; 197: 105696. doi: 10.1016/j.cmpb.2020.105696

12. Zhou C, Chase JG, Knopp J, et al. Virtual patients for mechanical ventilation in the intensive care unit. *Computer Methods and Programs in Biomedicine* 2021; 199: 105912. doi: 10.1016/j.cmpb.2020.105912

13. Sundaresan A, Chase JG, Shaw GM, Chiew YS, Desaive T. Model-based optimal PEEP in mechanically ventilated ARDS patients in the Intensive Care Unit. *BioMedical Engineering Online* 2011; 10(Mv): 1–18. doi: 10.1186/1475-925X-10-64

14. Sundaresan A, Yuta T, Hann CE, Geoffrey Chase J, Shaw GM. A minimal model of lung mechanics and model-based markers for optimizing ventilator treatment in ARDS patients. *Computer Methods and Programs in Biomedicine* 2009; 95(2): 166–180. doi: 10.1016/j.cmpb.2009.02.008

15. Bates JH, Irvin CG. Time dependence of recruitment and derecruitment in the lung: A theoretical model. *Journal of Applied Physiology* 2002; 93(2): 705–713. doi: 10.1152/japplphysiol.01274.2001

16. Ma B, Suki B, Bates JH. Effects of recruitment/derecruitment dynamics on the efficacy of variable ventilation. *Journal of Applied Physiology* 2011; 110(5): 1319–1326. doi: 10.1152/japplphysiol.01364.2010

17. Massa CB, Allen GB, Bates JH. Modeling the dynamics of recruitment and derecruitment in mice with acute lung injury. *Journal of Applied Physiology* 2008; 105(6): 1813–1821. doi: 10.1152/japplphysiol.90806.2008

18. Ma B, Bates JH. Modeling the complex dynamics of derecruitment in the lung. *Annals of Biomedical Engineering* 2010; 38(11): 3466–3477. doi: 10.1007/s10439-010-0095-2

19. Smith BJ, Lundblad LKA, Kollisch-Singule M, et al. Predicting the response of the injured lung to the mechanical breath profile. *Journal of Applied Physiology* 2015; 118(7): 932–940. doi: 10.1152/japplphysiol.00902.2014

20. Broche L, Perchiazzi G, Porra L, et al. Dynamic Mechanical Interactions between Neighboring Airspaces Determine Cyclic Opening and Closure in Injured Lung. *Critical Care Medicine* 2017; 45(4): 687–694. doi: 10.1097/CCM.0000000000002234

21. Knudsen L, Lopez-Rodriguez E, Berndt L, et al. Alveolar micromechanics in bleomycin-induced lung injury. *American Journal of Respiratory Cell and Molecular Biology* 2018; 59(6): 757–769. doi: 10.1165/rcmb.2018-0044OC

22. Smith BJ, Grant KA, Bates JH. Linking the development of ventilator-induced injury to mechanical function in the lung. *Annals of Biomedical Engineering* 2013; 41(3): 527–536. doi: 10.1007/s10439-012-0693-2

23. Hamlington KL, Smith BJ, Allen GB, Bates JHT. Predicting ventilator-induced lung injury using a lung injury cost function. *Journal of Applied Physiology* 2016; 121(1): 106–114. doi: 10.1152/japplphysiol.00096.2016

24. Roth CJ, Becher T, Frerichs I, Weiler N, Wall WA. Coupling of EIT with computational lung modeling for predicting patient-specific ventilatory responses. *Journal of Applied Physiology* 2017; 122(4): 855–867. doi: 10.1152/japplphysiol.00236.2016

25. Roth CJ, Ismail M, Yoshihara L, Wall WA. A comprehensive computational human lung model incorporating inter-acinar dependencies: Application to spontaneous breathing and mechanical ventilation. *International Journal for Numerical Methods in Biomedical Engineering* 2017; 33(1): 1–24. doi: 10.1002/cnm.2787

26. Ismail M, Comerford A, Wall WA. Coupled and reduced dimensional modeling of respiratory mechanics during spontaneous breathing. *International Journal for Numerical Methods in Biomedical Engineering* 2013; 29(11): 1285–1305. doi: 10.1002/cnm.2577

27. Becher T, Buchholz V, Hassel D, et al. Individualization of PEEP and tidal volume in ARDS patients with electrical impedance tomography: a pilot feasibility study. *Annals of Intensive Care* 2021; 11(1): 89. doi: 10.1186/s13613-021-00877-7

28. Howatson Tawhai M, Pullan AJ, Hunter PJ. Generation of an Anatomically Based Three-Dimensional Model of the Conducting Airways. *Annals of Biomedical Engineering* 2000; 28(7): 793–802. doi: 10.1114/1.1289457

29. Weibel ER. *Morphometry of the Human Lung*. Berlin, Heidelberg: Springer Berlin Heidelberg . 1963

30. Horsfield K, Dart G, Olson DE, Filley GF, Cumming G. Models of the human bronchial tree.. *Journal of Applied Physiology* 1971; 31(2): 207–217. doi: 10.1152/jappl.1971.31.2.207

31. Majumdar A, Alencar AM, Buldyrev SV, et al. Relating airway diameter distributions to regular branching asymmetry in the lung. *Physical Review Letters* 2005; 95(16): 2–5. doi: 10.1103/PhysRevLett.95.168101

32. Naureckas ET, Dawson CA, Gerber BS, et al. Airway reopening pressure in isolated rat lungs. *Journal of Applied Physiology* 1994; 76(3): 1372–1377. doi: 10.1152/jappl.1994.76.3.1372

33. Van Oss CJ, Absolom DR, Neumann AW, Zingg W. Determination of the surface tension of proteins I. Surface tension of native serum proteins in aqueous media. *BBA - Protein Structure* 1981; 670(1): 64–73. doi: 10.1016/0005-2795(81)90049-0

34. Bilek AM, Dee KC, Gaver DP. Mechanisms of surface-tension-induced epithelial cell damage in a model of pulmonary airway reopening. *Journal of Applied Physiology* 2003; 94(2): 770–783. doi: 10.1152/japplphysiol.00764.2002

35. Widdicombe JH. Regulation of the depth and composition of airway surface liquid. *Journal of Anatomy* 2002; 201(4): 313–318. doi: 10.1046/j.1469-7580.2002.00098.x

36. Markstaller K, Kauczor HU, Weiler N, et al. Lung density distribution in dynamic CT correlates with oxygenation in ventilated pigs with lavage ARDS. *British Journal of Anaesthesia* 2003; 91(5): 699–708. doi: 10.1093/bja/aeg246

37. Ogden RW, A PRSL. Large deformation isotropic elasticity – on the correlation of theory and experiment for incompressible rubberlike solids. *Proceedings of the Royal Society of London. A. Mathematical and Physical Sciences* 1972; 326(1567): 565–584. doi: 10.1098/rspa.1972.0026

38. Gattinoni L, Caironi P, Pelosi P, Goodman LR. What has computed tomography taught us about the acute respiratory distress syndrome?. *American Journal of Respiratory and Critical Care Medicine* 2001; 164(9): 1701–1711. doi: 10.1164/ajrccm.164.9.2103121

39. Pelosi P, D'Andrea L, Vitale G, Pesenti A, Gattinoni L. Vertical gradient of regional lung inflation in adult respiratory distress syndrome. *American Journal of Respiratory and Critical Care Medicine* 1994; 149(1): 8–13. doi: 10.1164/ajrccm.149.1.8111603

40. Yoshida T, Amato MB, Grieco DL, et al. Esophageal manometry and regional transpulmonary pressure in lung injury. *American Journal of Respiratory and Critical Care Medicine* 2018; 197(8): 1018–1026. doi: 10.1164/rccm.201709-1806OC

41. West JB, Luks A. *West's Respiratory Physiology - The Essentials*. Warszawa: Wolters Kluwer . 2016.

42. Gattinoni L, Marini JJ, Collino F, et al. The future of mechanical ventilation: Lessons from the present and the past. *Critical Care* 2017; 21(1): 1–11. doi: 10.1186/s13054-017-1750-x

43. Protti A, Cressoni M, Santini A, et al. Lung stress and strain during mechanical ventilation: Any safe threshold?. *American Journal of Respiratory and Critical Care Medicine* 2011; 183(10): 1354–1362. doi: 10.1164/rccm.201010-1757OC

44. Smith BJ, Bates JH. Variable Ventilation as a Diagnostic Tool for the Injured Lung. *IEEE Transactions on Biomedical Engineering* 2015; 62(9): 2106–2113. doi: 10.1109/TBME.2014.2315964

45. Ma H, Fujioka H, Halpern D, Gaver DP. Surfactant-Mediated Airway and Acinar Interactions in a Multi-Scale Model of a Healthy Lung. *Frontiers in Physiology* 2020; 11(August): 1–16. doi: 10.3389/fphys.2020.00941

46. Ryans J, Fujioka H, Halpern D, Gaver DP. Reduced-Dimension Modeling Approach for Simulating Recruitment/Derecruitment Dynamics in the Lung. *Annals of Biomedical Engineering* 2016; 44(12): 3619–3631. doi: 10.1007/s10439-016-1672-9

47. Ghadiali S, Huang Y. Role of Airway Recruitment and Derecruitment in Lung Injury. *Critical Reviews™ in Biomedical Engineering* 2011; 39(4): 297–318. doi: 10.1615/CritRevBiomedEng.v39.i4.40

48. Seeger W, Günther A, Walmrath HD, Grimminger F, Lasch HG. Alveolar surfactant and adult respiratory distress syndrome - Pathogenetic role and therapeutic prospects. *The Clinical Investigator* 1993; 71(3): 177–190. doi: 10.1007/BF00180100

49. Biehler J, Gee MW, Wall WA. Towards efficient uncertainty quantification in complex and large-scale biomechanical problems based on a Bayesian multi-fidelity scheme. *Biomechanics and Modeling in Mechanobiology* 2015; 14(3): 489–513. doi: 10.1007/s10237-014-0618-0

50. Wirthl B, Brandstaeter S, Nitzler J, Schrefler BA, Wall WA. Global sensitivity analysis based on Gaussian-process metamodelling for complex biomechanical problems. *arXiv:2202.01503 [stat.AP]* 2022. https://arxiv.org/abs/2202.01503. Accessed November 29, 2022.

51. Albert SP, DiRocco J, Allen GB, et al. The role of time and pressure on alveolar recruitment. *Journal of Applied Physiology* 2009; 106(3): 757–765. doi: 10.1152/japplphysiol.90735.2008

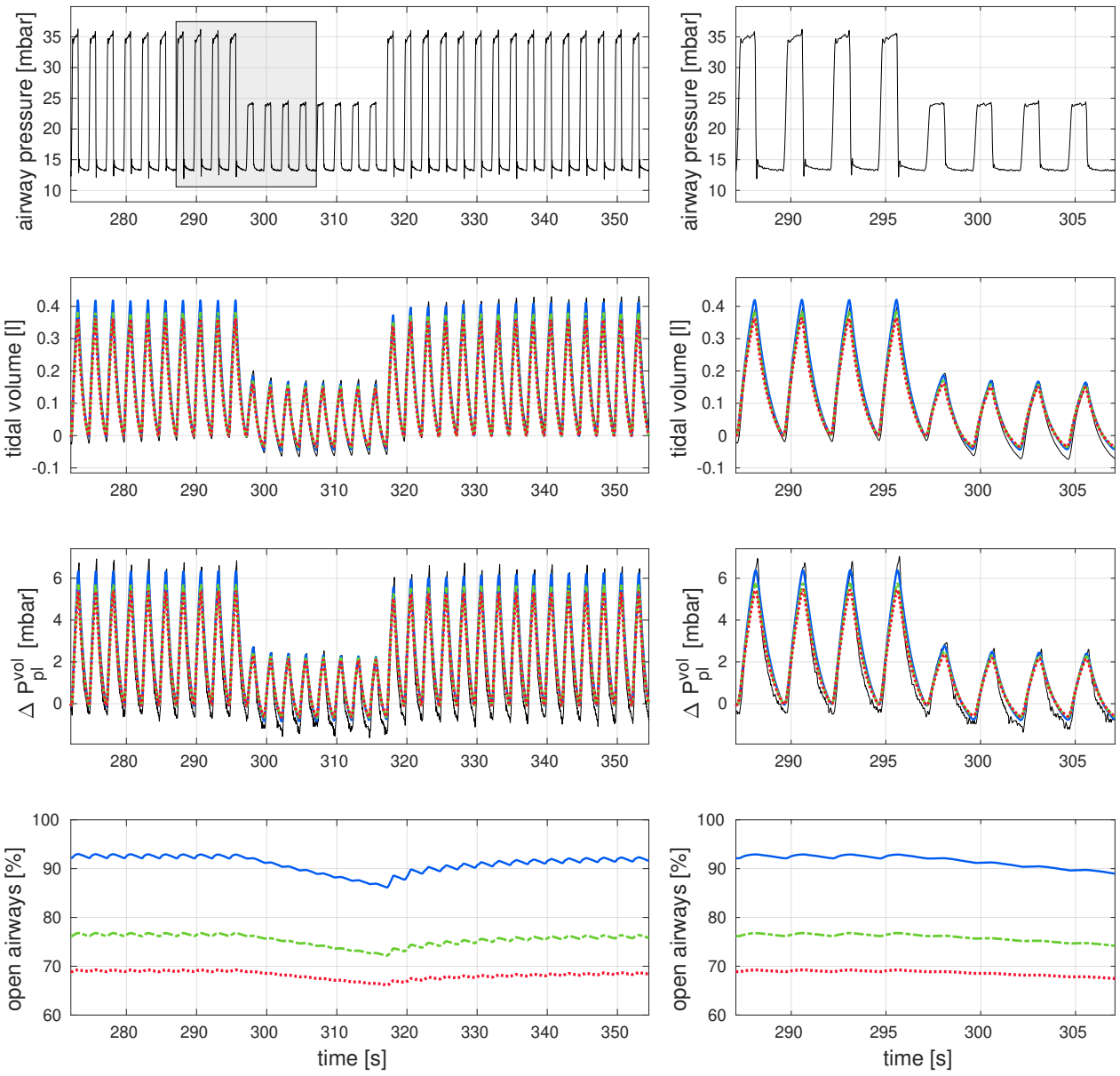

FIGURE 7 Simulation results of the proposed computational model for a clinically applied airway pressure profile of normal ventilation with temporarily halved driving pressure (top) for all three scenarios of surface tension γ, 70 dyn/cm (blue solid), 100 dyn/cm (green dashed) and 130 dyn/cm (red dotted) from top to bottom: tidal volume and change in pleural pressure compared to the clinical measurements (black solid), and the percentage of open airways in the whole model; in each figure, the area highlighted in grey (top left) indicates the period shown in more detail in the right column for all mentioned measures.

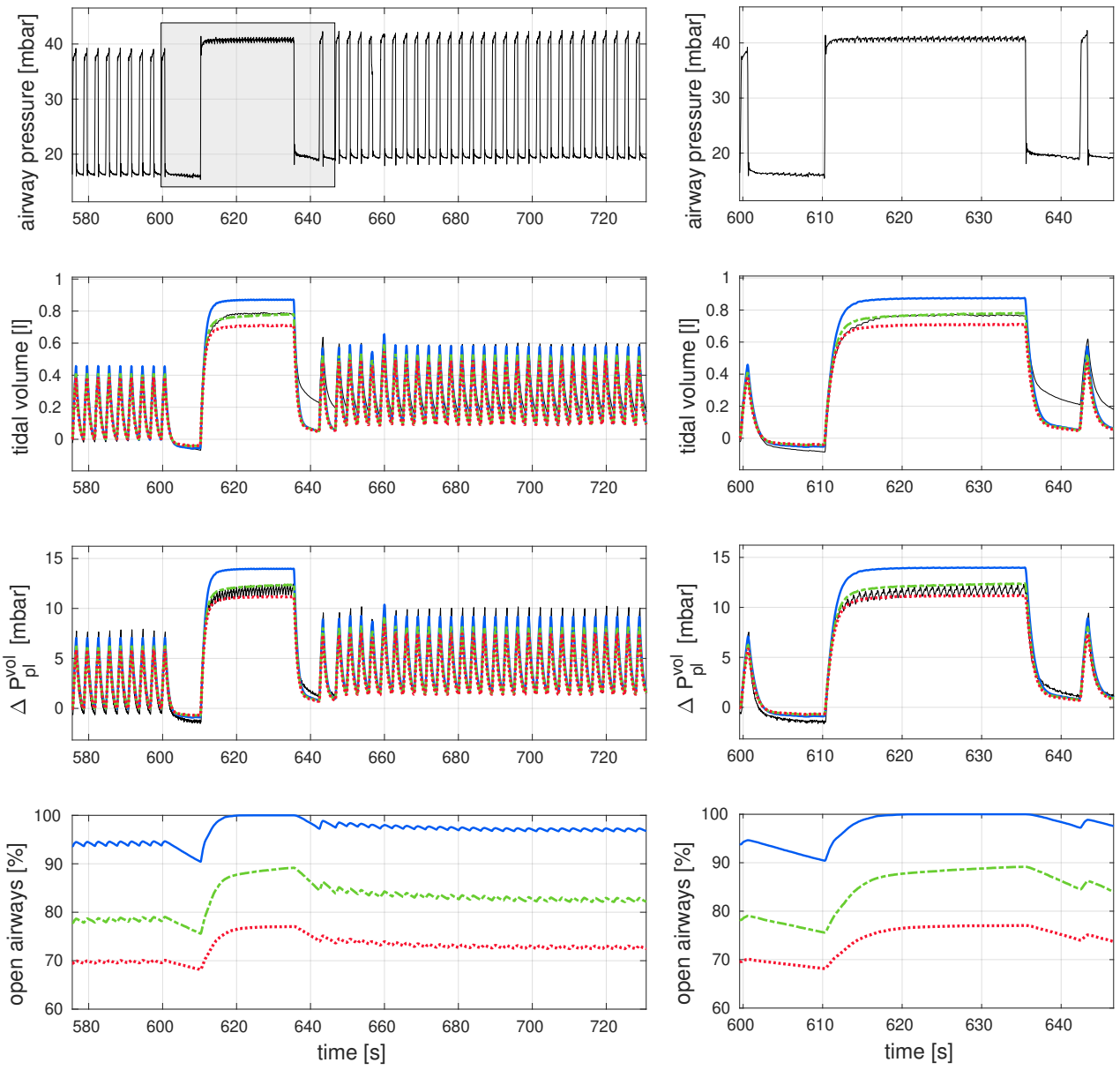

FIGURE 8 Simulation results of the proposed computational model for a clinically applied airway pressure profile containing a sustained-inflation recruitment maneuver (top) for all three scenarios of surface tension γ, 70 dyn/cm (blue solid), 100 dyn/cm (green dashed) and 130 dyn/cm (red dotted) from top to bottom: tidal volume and change in pleural pressure compared to the clinical measurements (black solid), and the percentage of open airways in the whole model; in each figure, the area highlighted in grey (top left) indicates the period shown in more detail in the right column for all mentioned measures.

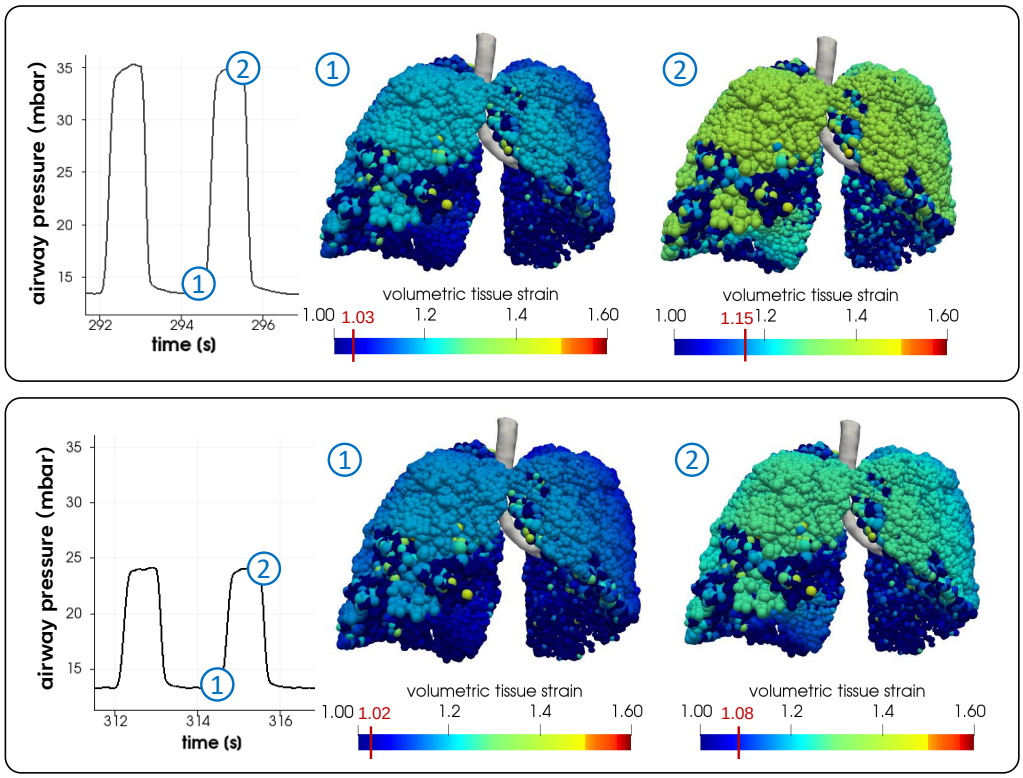

FIGURE 9 Local tissue strain of normal ventilation and halved driving pressure for $\gamma = 100$ dyn/cm, at end-expiration ($t = 294.5s$ and $t = 314.5s$, respectively; ①) and at end-inspiration ($t = 295.5s$ and $t = 315.5s$, respectively; ②). The distension of an exemplary ventral terminal unit, subjected to stronger straining due to position, differs for the models with surface tension 70 dyn/cm and 130 dyn/cm from the $\gamma = 100$ dyn/cm scenario by -1.67% and 0.0% at end-expiration (①), and by -2.92% and 1.46% at end-inspiration (②) during normal ventilation, respectively; during halved driving pressure, the strain deviates by -0.85% and 0.85% at end-expiration (①), and by -2.36% and 2.36% at end-inspiration (②), respectively.

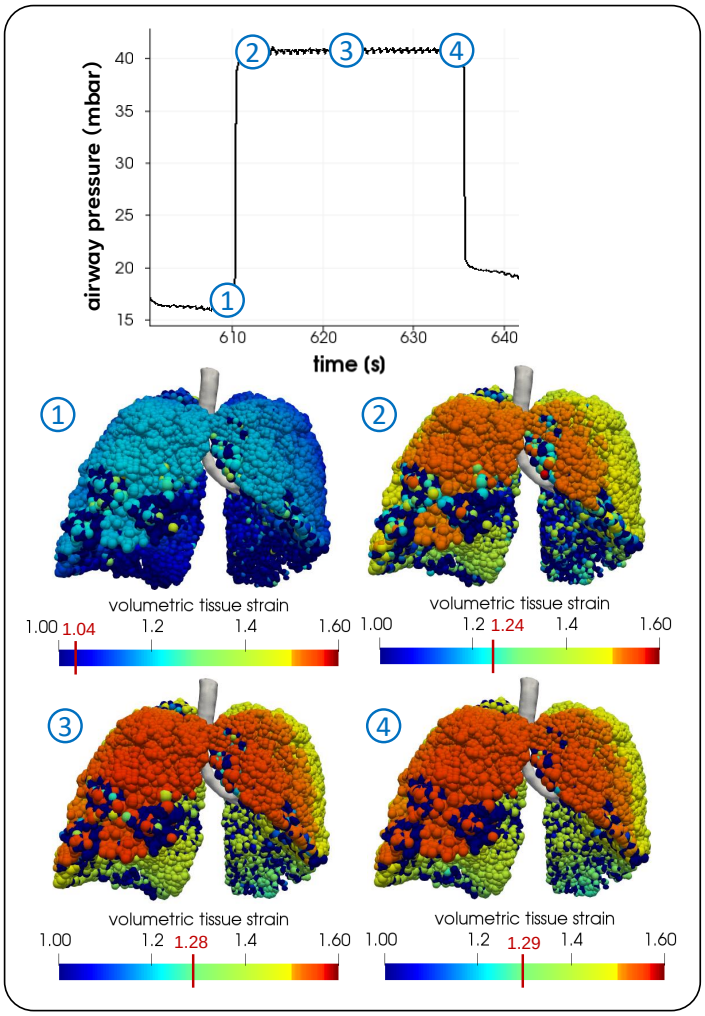

FIGURE 10 Local tissue strain during sustained-inflation maneuver for $\gamma = 100$ dyn/cm, before ($t = 610s$, ①), right after onset ($t = 612s$, ②), in the middle ($t = 623s$, ③) and at the end ($t = 635s$, ④) of the elevated pressure level. The distension of an exemplary ventral terminal unit, subjected to stronger straining due supine body, differs for the models with surface tension 70 dyn/cm and 130 dyn/cm from the $\gamma = 100$ dyn/cm scenario by -0.84% and 0.84% before (①), and -4.52% and 3.23% at the end (④) of the maneuver, respectively.

TABLE 1 Patient-specific parameters of the proposed computational model.

	Parameter	Value	Units
Terminal units	κ	3.7	mbar
(Ogden material)	β	−2.4	-
Chest wall	$P_{\mathrm{pl},0}$	10.15	mbar
	$P_{\mathrm{pl,lin}}$	9.35	mbar